Design of a simple bifunctional system as a self-assembled monolayer (SAM) for inverted tin-based perovskite solar cells

Atika Abid [a], Parameswaran Rajamanickam [b], Eric Wei-Guang Diau [a,c,*]

[a] *Department of Applied Chemistry and Institute of Molecular Science, National Yang Ming Chiao Tung University, 1001 Ta-Hseuh Rd., Hsinchu 300093, Taiwan*
[b] *Department of Materials Science and Engineering, National Yang Ming Chiao Tung University, 1001 Ta-Hseuh Rd., Hsinchu 300093, Taiwan*
[c] *Center for Emergent Functional Matter Science, National Yang Ming Chiao Tung University, 1001 Ta-Hseuh Rd., Hsinchu 300093, Taiwan*

ARTICLE INFO

ABSTRACT

In this work, we functionalized the ITO substrates with a series of self-assembled monolayer (SAM) molecules to improve the hole extraction ability of the electrodes and retard the charge recombination with the devices in an inverted planar p-i-n configuration. Organic molecules with simple structures, namely 4-aminobenzoic acid (AB), 4-(2-aminomethyl)benzoic acid (AM), 4-(2-aminoethyl)benzoic acid (AE), and 4-nitrobenzoic acid (NB) were chosen to functionalize the ITO substrates via simple immersion method to form hole-selective SAM on ITO. The TPSCs were fabricated according to a two-step sequential deposition approach using a co-solvent system, and the AB device was found to exhibit an attractive efficiency of power conversion (PCE) of 7.6 % while the other SAM-based devices showed poorer performance. The AB device also displayed impressive long-term storage stability by maintaining about 80 % of its initial efficiency for over 3500 h without encapsulation, in addition to a long-term (6 h) light-soaking stability, which is superior to the PEDOT: PSS-based device in ambient conditions. The SAM/perovskite interfacial characteristics were studied using UPS, EIS, and TCSPC to understand the energy levels, charge recombination, and hole-extraction nature, respectively, and to support the outstanding performance and stability of the AB device.

1. Introduction

Tin-based perovskites have been considered a promising environmentally benign sustainable alternative against lead-based analogs for photovoltaic applications [1–3]. Although recent growth in tin-based perovskite solar cells (TPSCs) has been impressive with the device power conversion efficiency (PCE) approaching 15 % [4], the high-performance TPSCs exclusively used the hydrophilic poly(3,4-ethylenedioxylenethiophene): poly(styrene sulfonic acid) (PEDOT: PSS) as a hole-transport material (HTM), which could degrade the device performance quickly, especially under long-term illumination. Thus, looking for stable non-PEDOT: PSS HTMs as alternatives is a good option to enhance the stability and performance of the TPSC devices [5–7]. We have recently demonstrated that PEDOT: PSS can be replaced by the hydrophobic poly-triaryl-amine (PTAA) via surface treatment through phenethyl ammonium iodide (PEAI) to obtain a remarkable PCE of 8.3 % [8]. This replacement was made possible by fabricating the devices according to the two-step sequential deposition technique developed previously to form a smooth tin perovskite layer with controlled crystallization kinetics [9]. In addition to PTAA as HTM, a new set of pyrrolopyrrole-based (PPr) polymers [10] and triphenyl-amine (TPA-) functionalized isomeric polythiophenes [11] were successfully designed and synthesized to serve as HTMs for TPSCs to attain a PCEs of 7.6 % and 8.6 %, respectively, with remarkable long-term enduring stabilities over 6000 and 4000 h, respectively, which opens a new door toward device performance optimization through interfacial engineering [12,13].

Facile self-assembly of organic monolayers (SAMs) functionalized on the surface of transparent ITO substrates are considered an effective approach to modify the surface properties of the electrodes [14–16]. The promising attributes of SAMs have been discussed in detail [17], which has inspired the recent research progress in TPSCs using SAMs as hole-selective interlayers. By tailoring the ITO surface states via simple thermal annealing [18,19], MeO-2PACz was allowed to anchor on ITO and modify the surface functionality leading to enhanced charge extraction, and improved carrier recombination kinetics when TPSCs were fabricated by employing the two-step fabrication approach [20]. Although, the devices yielded a moderate PCE of 6.5 %, the role of the

tunable surface functionalities of the ITO electrodes was revealed from that study, and it was the first example of applying SAM as a hole-selective interlayer for TPSCs [20]. Later, X-shaped quinoxaline-based p-type organic dyes with π-extended thiophene conjugated units were synthesized to match the energy levels of tin perovskites, and to serve as hole-selective SAM for TPSCs to attain a PCE of 8.3 % [21], which is a new milestone in TPSC research using SAM to replace the commonly employed polymeric HTMs.

The design of a SAM system for an inverted TPSC has three requirements. First, an electron-withdrawing group (acceptor) as an anchor to attach to the ITO surface [22,23]. Second, the electron-donating group (donor) to interact with the tin-perovskite layer [24]. Third, a linker to connect between the donor and acceptor groups [25]. For this reason, a simple donor–acceptor system as SAM for TPSC was designed in the present study. The idea was to introduce the carboxyl group (–COOH) as an acceptor and the amino group (–NH$_2$) as a donor with benzene or its derivative as a linker between donor and acceptor. As a result, four SAM molecules in this series, namely 4-aminobenzoic acid (AB), 4-(2-aminomethyl)benzoic acid (AM), 4-(2-aminoethyl)benzoic acid (AE), and nitrobenzoic acid (NB) with the chemical structures shown in Fig. 1, were designed. The AB and NB molecules have the π-conjugated structures with the donor-π-acceptor and acceptor-π-acceptor configurations, respectively; the AM and AE molecules were designed according to AB, but with extended methyl and ethyl groups between the phenyl ring and the amino group, respectively. The carboxyl group-based molecules are selected herein rather than the usual phosphonic acid (-PO(OH)$_2$) groups to anchor on the surface of ITO due to the higher reactivity of the former with preferred adsorption on ITO surfaces [22]. In addition, the highly polarized nature of the carbonyl group, as compared to the phosphonic acid groups, allow them to readily form strong covalent bonds with the substrate, thereby providing a stable attachment, while the smaller footprints of the carboxyl groups enable greater surface coverage, denser molecular packing with reduced defects and improved monolayer integrity, thereby providing favorable interfacial characteristics [21,26]. These SAM molecules were dip-coated on the ITO substrates to fabricate TPSC devices in the inverted planar p-i-n configuration according to a two-step approach [9]. Among all the SAM-based devices, the AB device displayed an attractive PCE of 7.6 % (Table 1) with an impressive long-term storage stability by retaining over 80 % of the initial PCE for over 3500 h. Further, the AB device is shown to exhibit a better light-soaking stability than the conventional PEDOT: PSS-based device when both the unencapsulated devices were exposed under one-sun irradiation for 6 h in ambient conditions. To understand why the AB device has the best performance and stability, the electrochemical impedance spectral (EIS), time-correlated single-photon-counting (TCSPC), and X-ray photoelectron spectral (XPS) studies of all samples were carried out for comparison.

Table 1

Photovoltaic parameters of the best-performing devices corresponding to Fig. 4c.

Device	Integrated J_{sc}	J_{sc} /mA cm^{-2}	V_{oc} /V	FF	PCE /%
AB	19.78	19.92	0.534	0.719	7.6
AM	17.89	17.83	0.530	0.561	5.3
AE	15.75	15.46	0.522	0.641	5.2
NB	13.83	13.96	0.532	0.610	4.5

2. Results and discussion

A simple substrate immersion methodology was applied to deposit the SAM molecules on the surfaces of the ITO glass substrates. By virtue of self-assembly, chemical adsorption of the molecular anchoring groups onto the substrate occurs slowly with appropriate orientation adjustment of the molecular chains giving rise to uniform monolayer formation with good coverage and strong adherence, rendering the immersion method attractive for robust SAM formation, in contrast to spin-coating which typically gives rise to unstable, non-uniform multilayered physiosorbed films [27,28]. Based on our previous work [20], prior to soaking the substrates in the SAM solution, we annealed the ITO substrates at 400 °C for 30 min under oxygen atmosphere to modify the surface states and to allow a uniform SAM growth with complete coverage (detailed experimental procedure is given in the supporting information). The functionalized ITO electrodes are named as ITO/AB, ITO/AM, ITO/AE and ITO/NB for the respective SAM molecules, and the eventually formed perovskite (PSK) films on the ITO/SAM electrodes are denoted as AB/PSK, AM/PSK, AE/PSK, and NB/PSK, respectively.

The surface wettability of the SAM-functionalized ITO substrates was evaluated using contact angle measurement to test the compatibility of the functionalization process to facilitate an interaction with the perovskite precursor solution. We dropped SnI$_2$/DMSO precursor solution on the ITO/SAM substrates and observed a slightly increasing trend in the contact angles (Fig. 2a-d). The smooth spread of the precursor solution associated with the lower contact angle, as in the case of ITO/AB (~6.52°), is highly desired to form a uniform perovskite layer [12]. Whereas, the contact angle of ITO/NB (~12.85°) was double that found in the NH$_2$-counterpart possibly due to the weaker hydrogen bonding ability of the –NO$_2$ group with the precursor solution [29]. Despite possessing almost identical surface morphology and similar roughness estimated using AFM (Fig. S1), the altered surface reactivity of the electrodes with the perovskite precursor led to pronounced changes in the formed perovskite grains. The SEM image of AB/PSK (Fig. 2e) shows large, uniform, and densely packed grains with minimal surface defects, indicative of possible regulation in perovskite nucleation and crystallization kinetics. In contrast, the AM/PSK (Fig. 2f) and AE/PSK (Fig. 2g)
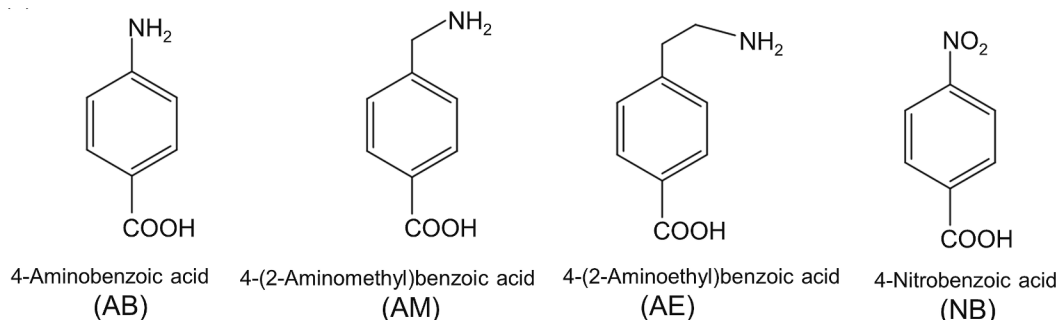

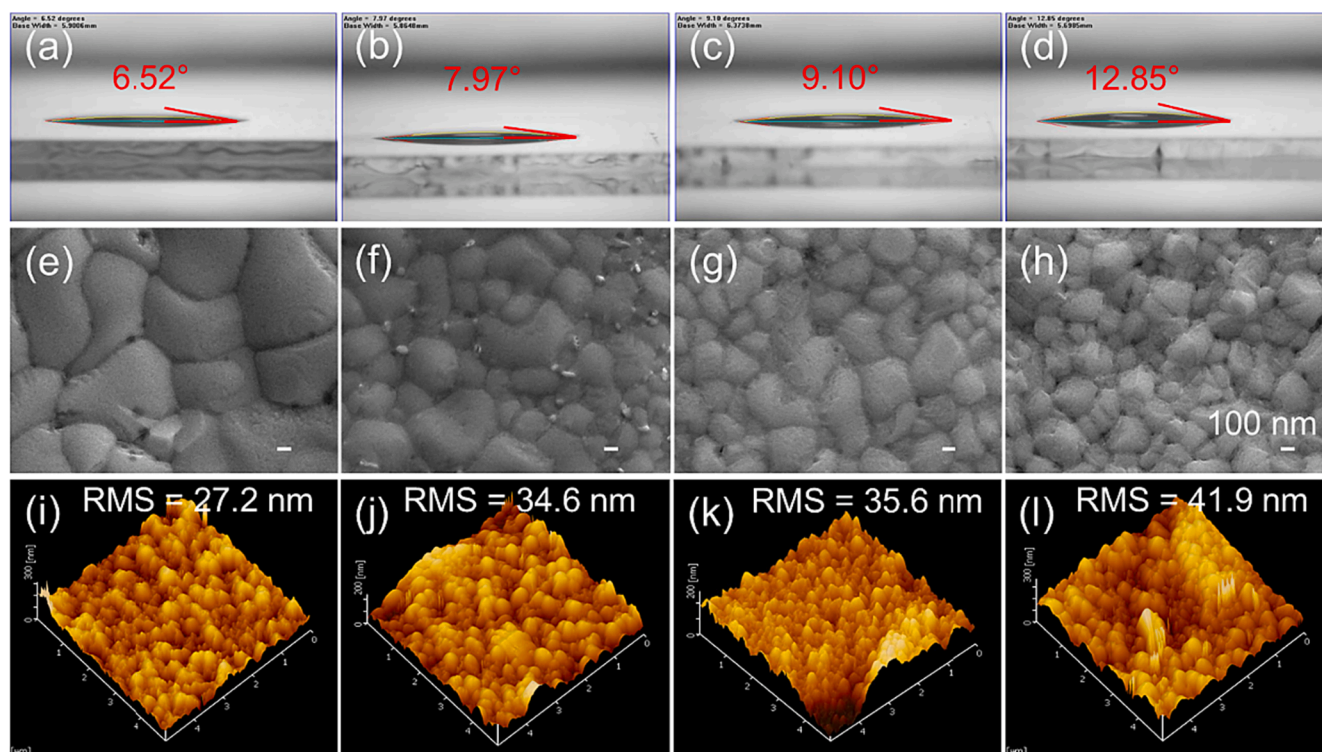**Fig. 1.** Chemical structures of the SAM molecules used in this study.

Fig. 2. Contact angles measured on (a) ITO/AB, (b) ITO/AM, (c) ITO/AE, and (d) ITO/NB substrates using SnI_2/DMSO precursor solution; SEM surface morphologies (e-h), and AFM roughness profiles (i-l) probed from the perovskite samples prepared over the functionalized electrodes (AB/PSK, AM/PSK, AE/PSK, and NB/PSK, respectively).

display considerable inhomogeneity in the grain size distribution as compared to that of AB/PSK. This could be due to the slight attenuation in the interaction brought about by both AM and AE between the ITO and the perovskite due to the extended chain lengths, which aligns well with the gradually increasing trend in the contact angle measurement (Fig. 2a-c). On the other hand, NB/PSK has the poorest surface morphology among all the samples with defective grains and inhomogeneous size distribution (Fig. 2h). The XRD patterns acquired from the SAM/PSK samples are shown in Fig. S2. The characteristic diffraction peaks associated with $FASnI_3$-based perovskites are accounted for (with the exposed facets marked), along with those of the ITO glass substrate (marked as #) [30]. The diffraction peak associated with the plane (1 0 0) of AB-, AM-, and AE-based perovskite samples are almost as intense as the ITO diffraction peak at ~ 36°, implying not only good surface coverage and thickness of the perovskite layer, but also its high crystallinity. Particularly, the AB/PSK sample has the sharpest (1 0 0) peak (FWHM ~ 0.139°, Table S1), while that of NB/PSK has a relatively broader peak (FWHM ~ 0.196°, Table S1) among all the samples. This suggests that the samples featuring –NH_2-based SAMs leads to larger grain formation with superior surface morphology as seen in Fig. 2e-g. It is concluded that the –NH_2 functional group functioned as nucleation sites and ensured controlled crystallization with well-regulated growth of perovskite crystal, that is lacking in the –NO_2-counterpart which leads to the defective perovskite formation as seen in Fig. 2h. In addition, the relative intensity between the (1 0 0) and (2 0 0) facets in AB/PSK maintains a 2:1 ratio implying a highly preferred orientation with uniform crystallization which leads to enriched optical properties. The surface topographies of the formed perovskite layers were probed using AFM (Fig. 2i-l), and the features correlate with the contact angle and SEM measurements with significantly smoother surface characteristics in AB/PSK than in the others. Furthermore, the SEM cross-sectional images of the SAM/PSK samples (Fig. S3) confirm the smoother uniform coating of perovskite layer on ITO/AB substrate with thicker films for the NH_2-based SAMs than for the NO_2-based film, arising from the

differences in the nucleation and crystallization kinetics of the perovskite on different ITO/SAM substrates consistent with the XRD measurements. Moreover, this defective perovskite layer formation of the NB/PSK sample could be the result of weaker interaction between the –NO_2 group of NB and Sn^{2+} ions of perovskite, which led to its film roughness with an rms of 41.9 nm that is much greater than that of the AB/PSK film (rms ~ 27.2 nm) [31].

The presence of the functional groups on the ITO surface was confirmed through X-ray photoelectron spectroscopy (XPS), with the spectra from ITO/AB possessing –NH_2 signal (~399 eV), and that of ITO/NB having –NO_2 signal (~406 eV), implying successful functionalization of SAMs on the ITO surface (Fig. S4) [32]. The Sn 3d XPS spectra of the perovskite samples are shown in Fig. 3. They were deconvoluted to obtain the relative proportions of Sn^{2+} and Sn^{4+}; the corresponding results are tabulated in Table S2. Accordingly, AB/PSK (Fig. 3a) possessed a highest Sn^{2+}/Sn^{4+} ratio (90.7/9.3), while the NB/PSK (Fig. 3d) possessed the lowest Sn^{2+}/Sn^{4+} ratio (74.7/25.3), with the AM/PSK (81.2/18.8, Fig. 3b) and AE/PSK (80.6/19.4, Fig. 3c) samples containing greater Sn^{2+} amounts than that of NB/PSK. The perovskite samples studied in this work include $EDAI_2$ as a co-additive whose role is to passivate the defective surface [30], and hence a high Sn^{2+}/Sn^{4+} ratio in AB/PSK is reasonable. Furthermore, the presence of –NH_2 group at the electrode/perovskite interface provides a reducible environment for perovskite [33], thereby ensuring a high Sn^{2+}/Sn^{4+} ratio. The Sn^{2+}/Sn^{4+} ratio in ITO/PSK was estimated to be 75.5/24.5 from Fig. 3e, which is slightly higher than that found in NB/PSK, while significantly lower than the samples featuring –NH_2-functionalized electrodes. This affirms the fact that the presence of –NH_2 at the electrode/perovskite interface provides a reducible environment to the tin-based perovskite. Whereas, the lower Sn^{2+} concentration in NB/PSK can be associated with the high electronegativity of the –NO_2 group at the electrode/perovskite interface which withdraws electrons from the perovskite, leaving holes to accelerate the Sn^{2+} oxidation. This also emphasizes the importance of strong electrode/perovskite interaction with the appropriate interlayers
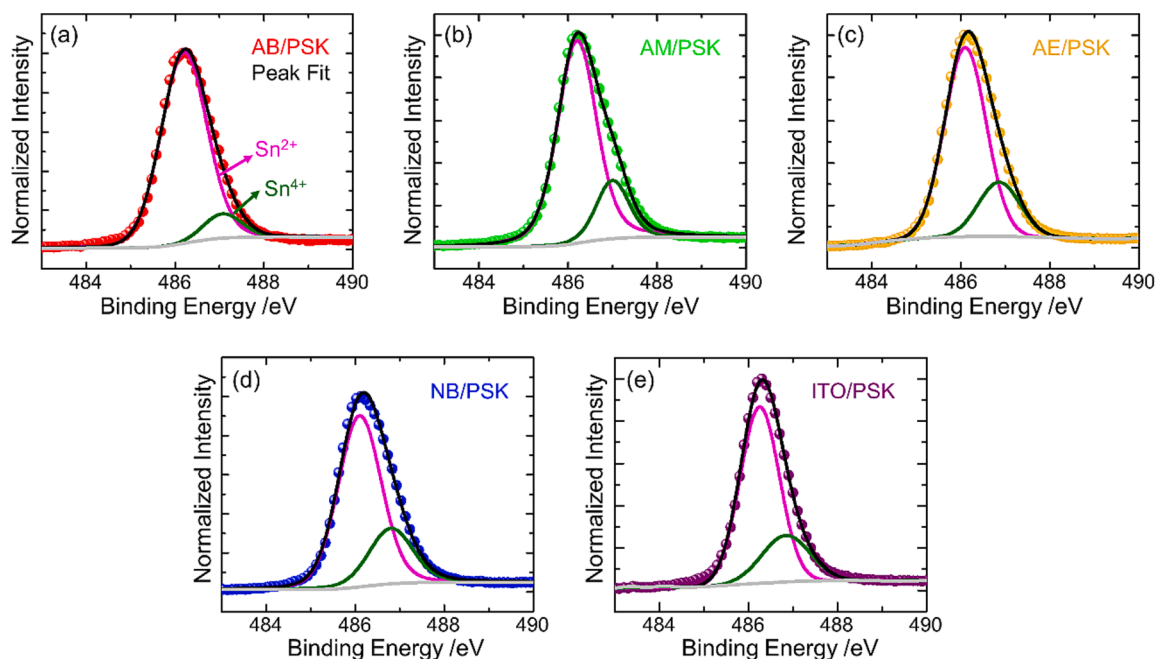
Fig. 3. High-resolution XPS spectra (Sn 3d) from the surface of perovskite samples (a) AB/PSK, (b) AM/PSK, (c) AE/PSK, (d) NB/PSK, and (e) ITO/PSK.

to overcome the chemical instabilities and defects for TPSCs fabricated without HTMs.

The UV–visible absorption spectra of the SAM solutions (Fig. S5a) show a red spectral shift for AB as compared to NB because of higher π-π electronic conjugation for the former than for the latter. While, for the methyl (AM-) and the ethyl (AE-) substituents, the π-conjugation breaks down leading to a blue spectral shift. In addition, the SAM-functionalized electrodes display broader transmittance than the bare

ITO substrate (Fig. S5b) with the transmittance extending to the near-IR region, which makes them more suitable for TPSC devices with narrow band gap. This broadband transmittance results from the modified oxygen vacancies of ITO after the thermal treatment prior to the SAM formation [20]. The absorption spectra of the SAM/PSK samples show similar band edge positions (Fig. S6a), and the steady-state PL spectra (Fig. S6b) were used to estimate the band gaps of the perovskite samples. The PL peak maxima correspond to a band gap of ~ 1.43 eV for all the
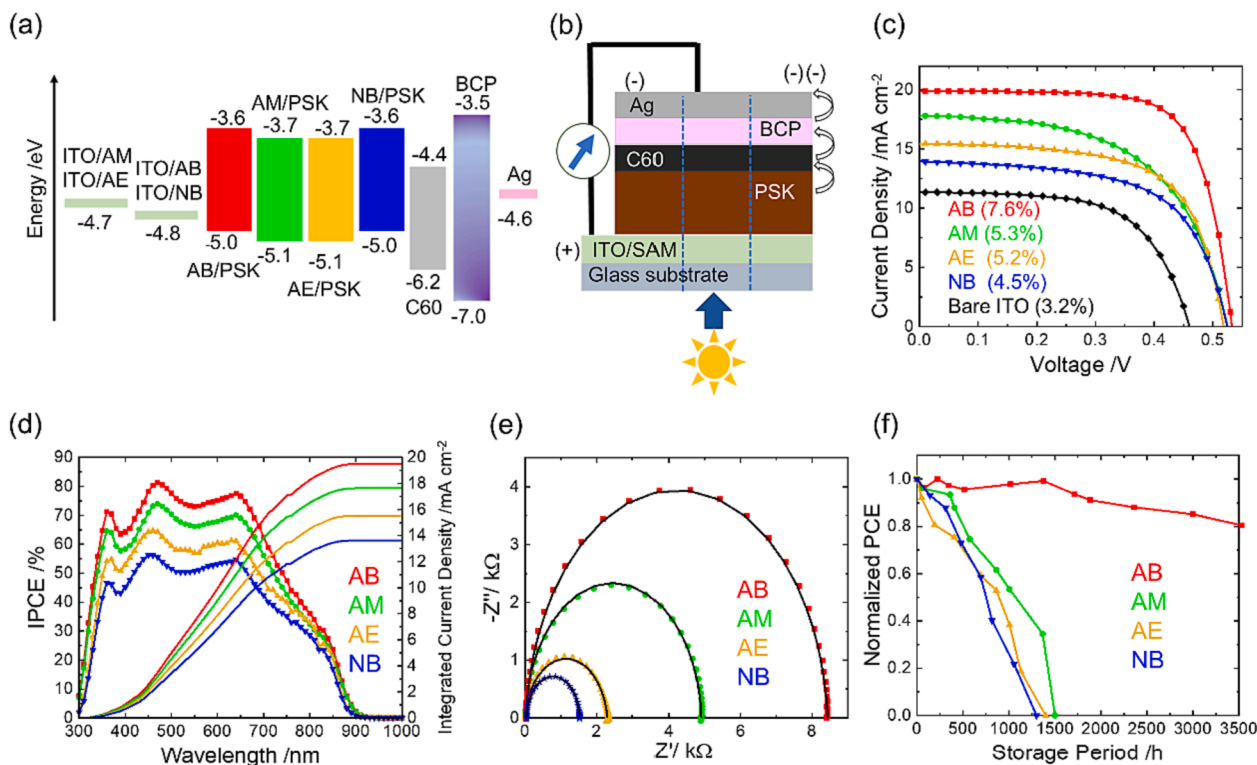

Fig. 4. (a) Device structure, (b) energy-level diagram, (c) *J-V* characteristics, (d) IPCE spectra, (e) EIS Nyquist plots and (f) long-term shelf-stability under dark for the devices made of AB, AM, AE and NB as indicated.

samples, agreeing with that of FASnI$_3$-based perovskite reported in the literature [34]. To test the energy alignment between the perovskite and the electrodes, ultra-violet photoelectron spectroscopy (UPS) was employed. Fig. S7 shows the UPS spectra recorded from the SAM-functionalized ITO electrodes. While the bare ITO glass is reported to have a work function of 4.7 eV [35], it slightly changes to ~ 4.8 eV for ITO/AB and ITO/NB, and remains unchanged for ITO/AM and ITO/AE. The surface properties of the functionalized substrates lead to the modulation in the valence band maximum (VBM) of the coated perovskite samples. Consequently, the VBM values of AB/PSK and NB/PSK were estimated to be −5.0 eV, while they were found to be −5.1 eV for AM/PSK and AE/PSK (Fig. S8), both are slightly deeper when compared to the previous reports [36,37]. Based on the calculated band gaps and the estimated VBM, we expect well-aligned energy levels for the different layers constituting a TPSC as shown in Fig. 4a.

We fabricated devices in the inverted planar p-i-n configuration (Fig. 4b) using the SAM-functionalized ITO electrodes to overcome the undesired charge transport and recombination routes [38] by employing the two-step fabrication method as reported elsewhere [9]. The *J-V* characteristic curves recorded from the best cells under one-sun AM 1.5G illumination is shown in Fig. 4c. As a result, the AB device displayed an outstanding device performance with a *J*sc of 19.92 mA cm^{-2}, *V*oc of 0.534 V, FF of 0.719, and PCE of 7.6 %. For the AB derivatives, AM and AE with additional alkyl chains to make the molecules more flexible than AB, a PCE of 5.3 % (AM) and 5.2 % (AE) were obtained. For the accepter-π-acceptor SAM, NB, despite having an energy alignment identical to that of the AB device, much poorer PCE (4.5 %) was obtained due to the much lower *J*sc (~13.96 mA cm^{-2}) for the NB device than for the AB device. All the SAM-based devices performed better in comparison to the device fabricated using bare ITO electrode after UV-ozone treatment (PCE = 3.2 %), which highlights the essentiality of functionalization via SAM [20,21] to serve as a buffer layer to enable carrier separation and extraction [8,10]. The incident photon-to-current conversion efficiency (IPCE) spectra were measured for the best cells to obtain the associated integrated photocurrent densities (Fig. 4d). The estimated integrated *J*sc values agree well with those obtained from the characteristic *J-V* curves with the order AB > AM > AE > NB. In particular, the NB device possess severely suppressed IPCE in comparison to the other devices, indicating attenuated charge collection which accounts for its poor *J*sc [39]. The decreasing trend in *J*sc from AB to NB device is consistent with the trend observed in the corresponding IPCE spectra. The spectral shapes are identical with substantial changes only in their intensities which are characteristics of the overall carrier generation ability at each wavelength. Note that the overall absorbance from 350 to 900 nm of the SAM/PSK samples (Fig. S6a) follow the similar trend being discussed here, and it aligns well with the perovskite layer thicknesses on different ITO/SAM (Fig. 3) electrodes. Hence, the uniform film formation with greater thickness and superior crystallinity (Fig. S2) with a trend of AB > AM > AE > NB is reflected in the IPCE spectra [40].

Despite having significant differences between the obtained *J*sc, the fabricated devices displayed similar *V*oc, arising from the minimal impact of ITO functionalization on tuning the work functions (Fig. S7), and also on the similar energy level alignments (Fig. 4a) [41]. The interfacial charge transport characteristics play a crucial role in defining the device stability in a long-term, especially for the ones lacking a carrier transport layer. Hence, we performed electrochemical impedance spectroscopy (EIS) [42] with the fabricated devices by biasing them at 0.5 V under darkness. The Nyquist plots (Fig. 4e) were fitted by applying an appropriate equivalent-circuit model for a comprehensive analysis of the charge transport and recombination processes [43]. The single semicircle encompassing the whole frequency range of the EIS measurements can be assigned to the charge recombination process as the charge carriers traverse [44]. The size of the semicircular spectra was used to estimate the resistance against the interfacial charge recombination, which is tabulated in Table S3. The charge

recombination resistances of these devices show a systematic trend with the order AB (4.39 kΩ) > AM (2.42 kΩ) > AE (1.11 kΩ) > NB (0.78 kΩ), which agrees with the trend of *J*sc and overall device performance shown in Fig. 4c and 4d. The EIS data suggest that the poor performance of the NB device is mainly due to the significantly suppressed recombination resistance. Since the –NO$_2$ group in NB is a strong electron withdrawing group [25], the presence of the same as an interlayer between the perovskite active layer and the electrode could induce electron extraction in addition to the desired hole extraction, which would easily trigger electron-hole recombination that degrades the device performance quickly. In contrast, in other push–pull SAMs, the –NH$_2$ group, being an electron-donating group [45], effectively extracts only the holes from the PSK. In addition, in comparison to AB, the AM and AE based devices possess reduced recombination resistance possibly due to the extended chain lengths that give rise to undesirable carrier leakage. As a result, the AB device exhibited the best performance among the other devices as confirmed by the EIS measurements.

The electrode/perovskite interfacial charge carrier kinetics were investigated through time-resolved PL decay measurements performed using time-correlated single-photon-counting (TCSPC) technique. The PL decay profiles obtained from both AB/PSK and NB/PSK were fitted with a single-exponential function, while those obtained from both AM/PSK and AE/PSK were fitted with a bi-exponential function (Fig. S9). The average PL lifetimes estimated from the fitted data (τ_1 only for AB/PSK and NB/PSK) along with the individual rapid- and slow-decay coefficients (τ_1 and τ_2 for AM/PSK and AE/PSK) [46] are tabulated in Table S4. The PL lifetimes show a systematic trend for AB/PSK (0.7 ns) < AM/PSK (2.6 ns) < AE/PSK (6.4 ns), indicating the hole extraction following the same trend. The additional alkyl chains in AM and AE retarded the hole extraction so that AB becomes the best SAM for TPSC. In contrast, the NB/PSK film shows much shorter PL lifetime (0.4 ns) due to two reasons. First, the poor film morphology shown in Fig. 2h with poor crystallinity (Fig. S2) indicates that more surface defects might be involved for the NB/PSK films than for the other films. This surface defect would quench PL intensity and lead to reduction in PL lifetime. Second, since NB involves –NO$_2$ group to effectively withdraw electrons from PSK, it was electrons rather than holes being extracted from PSK to NB with much shorter PL lifetime. This electron extraction characteristic in NB led to charge recombination as observed in the EIS results. Therefore, much poorer J_{SC} and PCE were observed for the NB device than for the other devices.

The effect of hysteresis of the AB device was assessed by sweeping the *J-V* curves in both reverse (*V*oc to 0 V) and forward (0 V to *V*oc) directions, which displayed negligible hysteresis (Fig. S10). The reproducibility of the SAM-based devices is displayed through the boxplots shown in Fig. S11, with the corresponding photovoltaic parameters being tabulated in Table S5-8; 25 devices in total for each SAM were fabricated at identical experimental conditions with an active area of 0.0225 cm^2. We also examined the effect of varied concentrations of the SAM solutions on the device performance of AB, and the corresponding data are shown in Fig. S12. Fig. S12a shows a marked reduction in the absorbance as we reduced the AB solution concentration from 1.0 mM to 0.1 mM. The *J-V* characteristic curves recorded from the devices fabricated using the corresponding SAM solution concentration are shown in Fig. S12b, which reveals an increasing trend in the PCE (0.5 % for 1.0 mM to 7.6 % for 0.1 mM solution). The trend is associated with the saturation in the absorption spectra at higher concentrations of AB (Fig. S12a) due to severe agglomeration of AB in high-concentration condition. To examine the long-term stability of the device, the fabricated devices were stored inside a nitrogen-filled glovebox, and the PCE was measured periodically as shown in Fig. 4f. The AB device exhibits an outstanding long-term stability with 80 % of the initial PCE being maintained even after a storage period of over 3500 h, while the other devices degraded quickly with the stability order AM > AE ~ NB; all three SAM devices with the PCE went down to naught after 1500 h of storage. In comparison to the newly reported polymer HTM-based

TPSCs, the device stability exhibited in our work stands out due to the non-involvement of any additional interlayer-pre-treatments on the SAM-functionalized ITO electrodes, making them truly HTM-free TPSC devices. However, the previously reported HTM-based devices demanded interlayer formation to tune the surface energy of the polymer layer itself to enable an interaction between the perovskite and the HTM/electrode [8,10,11]. Additionally, we tested the light-soaking stability of the AB device in ambient conditions (relative humidity $\sim$ 60 %) without encapsulation and compared its performance against a conventional PEDOT: PSS-based device (Fig. S13) by measuring the device performance at the maximum power point under simulated AM 1.5G illumination for about 6 h. We noticed a quicker degradation of the PEDOT: PSS-based device under light illumination in comparison to the AB device. The latter was able to withstand the harsh effects of both thermal stress and light soaking, implying its superior photo- and thermal-stability relative to the conventional HTMs. This is for the first time a TPSC based on such a simple SAM (aminobenzoic acid) as a hole-selective interlayer with decent device performance and stability being reported.

3. Conclusion

We designed a new series of simple self-assembled monolayer (SAM) molecules with bifunctional groups to replace the moisture-sensitive PEDOT: PSS as HTM for inverted tin perovskite solar cells (TPSCs). The idea was to introduce benzene as a core molecule, together with an electron-withdrawing group (acceptor; carboxylic acid) on one side and an electron-donating group (donor; amine) on the other side to form a SAM molecule with an acceptor-π-donor configuration. The first SAM is aminobenzoic acid (AB), which exhibited outstanding hole-extraction ability with retarded charge recombination to attain the best device performance with PCE 7.6 % according to a two-step device fabrication approach. Methyl and ethyl substituents were introduced between benzene and amino moiety to increase the flexibility of the SAM to interact with the tin perovskite layer. However, insertion of a non-conjugated alkyl chain in SAM reduced the ability of hole extraction, leading to a systematic reduction in J_{SC} that degraded the device performance. When the amino group in AB was replaced by an electron-withdrawing acceptor like a nitro group (NB), the electron extraction from perovskite to NB took place which facilitated significant interfacial charge recombination to reduce J_{SC} further for NB to become the poorest device among all the SAM-based TPSCs. The AB device also displayed outstanding long-term stability to maintain 80 % of its initial PCE for over 3500 h without encapsulation in dark. Under light-soaking condition, the AB-based TPSC was also superior to the PEDOT: PSS device with the perovskite layer fabricated under the same experimental condition.

Declaration of Competing Interest

The authors declare the following financial interests/personal relationships which may be considered as potential competing interests: Eric Wei-Guang Diau reports a relationship with Ministry of Science and Technology, Taiwan that includes: funding grants.

Data availability

Data will be made available on request.

Acknowledgements

Appendix A. Supplementary data

Supplementary data to this article can be found online at https://doi.org/10.1016/j.cej.2023.146755.

References

[1] A. Toshniwal, V. Kheraj, Development of organic-inorganic tin halide perovskites: a review, Sol. Energy 149 (2017) 54–59, https://doi.org/10.1016/j.solener.2017.03.077.

[2] X. Liu, T. Wu, X. Luo, H. Wang, M. Furue, T. Bessho, Y. Zhang, J. Nakazaki, H. Segawa, L. Han, Lead-free perovskite solar cells with over 10% efficiency and size 1 cm2 enabled by solvent-crystallization regulation in a two-step deposition method, ACS Energy Lett. 7 (2022) 425–431, https://doi.org/10.1021/acsenergylett.1c02651.

[3] K. Nishimura, M.A. Kamarudin, D. Hirotani, K. Hamada, Q. Shen, S. Iikubo, T. Minemoto, K. Yoshino, S. Hayase, Lead-free tin-halide perovskite solar cells with 13% efficiency, Nano Energy 74 (2020), 104858, https://doi.org/10.1016/j.nanoen.2020.104858.

[4] X. Jiang, H. Li, Q. Zhou, Q. Wei, M. Wei, L. Jiang, Z. Wang, Z. Peng, F. Wang, Z. Zang, K. Xu, Y. Hou, S. Teale, W. Zhou, R. Si, X. Gao, E.H. Sargent, Z. Ning, One-step synthesis of SnI2·(DMSO)xAdducts for high-performance tin perovskite solar cells, J. Am. Chem. Soc. 143 (2021) 10970–10976, https://doi.org/10.1021/jacs.1c03032.

[5] A. Abate, Stable tin-based perovskite solar cells, ACS Energy Lett. 8 (2023) 1896–1899, https://doi.org/10.1021/acsenergylett.3c00282.

[6] W. Han, G. Ren, J. Liu, Z. Li, H. Bao, C. Liu, W. Guo, Recent progress of inverted perovskite solar cells with a modified PEDOT:PSS hole transport layer, ACS Appl. Mater. Interfaces 12 (2020) 49297–49322, https://doi.org/10.1021/acsami.0c13576.

[7] J. Cameron, P.J. Skabara, The damaging effects of the acidity in PEDOT:PSS on semiconductor device performance and solutions based on non-acidic alternatives, Mater. Horizons. 7 (2020) 1759–1772, https://doi.org/10.1039/c9mh01745g.

[8] C.-H. Kuan, G.-S. Luo, S. Narra, S. Maity, H. Hiramatsu, Y.-W. Tsai, J.-M. Lin, C.-H. Hou, J.-J. Shyue, E.-W.-G. Diau, How can a hydrophobic polymer ptaa serve as a hole- transport layer for an inverted tin perovskite solar cell? Chem. Eng. 450 (2022), 138037 https://doi.org/10.2139/ssrn.4110650.

[9] S. Shahbazi, M.Y. Li, A. Fathi, E.W.G. Diau, Realizing a cosolvent system for stable tin-based perovskite solar cells using a two-step deposition approach, ACS Energy Lett. 5 (2020) 2508–2511, https://doi.org/10.1021/acsenergylett.0c01190.

[10] C. Kuan, R. Balasaravanan, S. Hsu, J. Ni, Y. Tsai, Z. Zhang, M. Chen, E.W. Diau, Dopant-free pyrrolopyrrole-based (PPr) polymeric hole-transporting materials for efficient tin-based perovskite solar cells with stability over 6000 h, Adv. Mater. 35 (2023) 2300681, https://doi.org/10.1002/adma.202300681.

[11] R. Balasaravanan, C.H. Kuan, S.M. Hsu, E.C. Chang, Y.C. Chen, Y.T. Tsai, M.L. Jhou, S.L. Yau, C.L. Liu, M.C. Chen, E.W.G. Diau, Triphenylamine (TPA)-functionalized structural isomeric polythiophenes as dopant free hole-transporting materials for tin perovskite solar cells, Adv. Energy Mater. 13 (2023) 2302047, https://doi.org/10.1002/aenm.202302047.

[12] A.N. Cho, N.G. Park, Impact of interfacial layers in perovskite solar cells, ChemSusChem 10 (2017) 3687–3704, https://doi.org/10.1002/cssc.201701095.

[13] W. Gao, P. Li, J. Chen, C. Ran, Z. Wu, Interface engineering in tin perovskite solar cells, Adv. Mater. Interfaces 6 (2019) 1901322, https://doi.org/10.1002/admi.201901322.

[14] K. Choi, H. Choi, J. Min, T. Kim, D. Kim, S.Y. Son, G.W. Kim, J. Choi, T. Park, A short review on interface engineering of perovskite solar cells: a self-assembled monolayer and its roles, Sol. RRL. 4 (2020) 1900251, https://doi.org/10.1002/solr.201900251.

[15] E. Aktas, N. Phung, H. Köbler, D.A. González, M. Méndez, I. Kafedjiska, S.H. Turren-Cruz, R. Wenisch, I. Lauermann, A. Abate, E. Palomares, Understanding the perovskite/self-assembled selective contact interface for ultra-stable and highly efficient p-i-n perovskite solar cells, Energ. Environ. Sci. 14 (2021) 3976–3985, https://doi.org/10.1039/d0ee03807e.

[16] A. Ullah, K.H. Park, H.D. Nguyen, Y. Siddique, S.F.A. Shah, H. Tran, S. Park, S.I. Lee, K.K. Lee, C.H. Han, K. Kim, S.J. Ahn, I. Jeong, Y.S. Park, S. Hong, Novel phenothiazine-based self-assembled monolayer as a hole selective contact for highly efficient and stable p-i-n perovskite solar cells, Adv. Energy Mater. 12 (2022) 2103175, https://doi.org/10.1002/aenm.202103175.

[17] F. Ali, C. Roldán-Carmona, M. Sohail, M.K. Nazeeruddin, Applications of self-assembled monolayers for perovskite solar cells interface engineering to address efficiency and stability, Adv. Energy Mater. 10 (2020) 2002989, https://doi.org/10.1002/aenm.202002989.

[18] C. Donley, D. Dunphy, D. Paine, C. Carter, K. Nebesny, P. Lee, D. Alloway, N.R. Armstrong, Characterization of indium-tin oxide interfaces using X-ray photoelectron spectroscopy and redox processes of a chemisorbed probe molecule: effect of surface pretreatment conditions, Langmuir 18 (2002) 450–457, https://doi.org/10.1021/la011101t.

[19] G. Gonçalves, E. Elangovan, P. Barquinha, L. Pereira, R. Martins, E. Fortunato, Influence of post-annealing temperature on the properties exhibited by ITO, IZO

and GZO thin films, Thin Solid Films 515 (2007) 8562–8566, https://doi.org/10.1016/j.tsf.2007.03.126.

[20] D. Song, S. Narra, M.Y. Li, J.S. Lin, E.W.G. Diau, Interfacial engineering with a hole-selective self-assembled monolayer for tin perovskite solar cells via a two-step fabrication, ACS Energy Lett. 6 (2021) 4179–4186, https://doi.org/10.1021/acsenergylett.1c02124.

[21] S.N. Afraj, C.H. Kuan, J.S. Lin, J.S. Ni, A. Velusamy, M.C. Chen, E.W.G. Diau, Quinoxaline-based X-shaped sensitizers as self-assembled monolayer for tin perovskite solar cells, Adv. Funct. Mater. (2023) 2213939, https://doi.org/10.1002/adfm.202213939.

[22] S.A. Jadhav, Self-assembled monolayers (SAMs) of carboxylic acids: an overview, Cent. Eur. J. Chem. 9 (2011) 369–378, https://doi.org/10.2478/s11532-011-0024-8.

[23] E. Arkan, E. Yalcin, M. Unal, M.Z.Y. Arkan, M. Can, C. Tozlu, S. Demic, Effect of functional groups of self assembled monolayer molecules on the performance of inverted perovskite solar cell, Mater. Chem. Phys. 254 (2020), 123435, https://doi.org/10.1016/j.matchemphys.2020.123435.

[24] A. De Bettencourt-Dias, S. Viswanathan, Nitro-functionalization and luminescence quantum yield of Eu(iii) and Tb(iii) benzoic acid complexes, J. Chem. Soc. Dalt. Trans. (2006) 4093–4103, https://doi.org/10.1039/b606970c.

[25] M. Can, A.K. Havare, H. Aydin, N. Yagmurcukardes, S. Demic, S. Icli, S. Okur, Electrical properties of SAM-modified ITO surface using aromatic small molecules with double bond carboxylic acid groups for OLED applications, Appl. Surf. Sci. 314 (2014) 1082–1086, https://doi.org/10.1016/j.apsusc.2014.05.181.

[26] L. Li, Y. Wu, E. Li, C. Shen, H. Zhang, X. Xu, G. Wu, M. Cai, W.H. Zhu, Self-assembled naphthalimide derivatives as an efficient and low-cost electron extraction layer for n-i-p perovskite solar cells, Chem. Commun. 55 (2019) 13239–13242, https://doi.org/10.1039/c9cc06345e.

[27] F. Schreiber, Structure and growth of self-assembling monolayers, Prog. Surf. Sci. 65 (2000) 151–257, https://doi.org/10.1016/S0079-6816(00)00024-1.

[28] D.K. Schwartz, Mechanisms and kinetics of self-assembled monolayer formation, Annu. Rev. Phys. Chem. 52 (2001) 107–137.

[29] M.M. Pereira, K.A. Kurnia, F.L. Sousa, N.J.O. Silva, J.A. Lopes-Da-Silva, J.A. P. Coutinho, M.G. Freire, Contact angles and wettability of ionic liquids on polar and non-polar surfaces, PCCP 17 (2015) 31653–31661, https://doi.org/10.1039/c5cp05873b.

[30] E. Jokar, C.H. Chien, A. Fathi, M. Rameez, Y.H. Chang, E.W.G. Diau, Slow surface passivation and crystal relaxation with additives to improve device performance and durability for tin-based perovskite solar cells, Energ. Environ. Sci. 11 (2018) 2353–2362, https://doi.org/10.1039/c8ee00956b.

[31] R. Qiao, L. Zuo, Self-assembly monolayers boosting organic-inorganic halide perovskite solar cell performance, J. Mater. Res. 33 (2018) 387–400, https://doi.org/10.1557/jmr.2017.477.

[32] P. Iqbal, K. Critchley, D. Attwood, D. Tunnicliffe, S.D. Evans, J.A. Preece, Chemical manipulation by X-rays of functionalized thiolate self-assembled monolayers on au, Langmuir 24 (2008) 13969–13976, https://doi.org/10.1021/la802244a.

[33] W. Feng, Y. Tan, M. Yang, Y. Jiang, B.X. Lei, L. Wang, W.Q. Wu, Small amines bring big benefits to perovskite-based solar cells and light-emitting diodes, Chem 8 (2022) 351–383, https://doi.org/10.1016/j.chempr.2021.11.010.

[34] S. Narra, E. Jokar, O. Pearce, C. Lin, A. Fathi, E.W. Diau, Femtosecond transient absorption spectra and dynamics of carrier relaxation of tin perovskites in the absence and presence of additives, J. Phys. Chem. Lett. 11 (2020) 5699–5704, https://doi.org/10.1021/acs.jpclett.0c01589.

[35] D. Song, L.Y. Hsu, C.M. Tseng, E.W.G. Diau, Solution-processed ITO nanoparticles as hole-selective electrodes for mesoscopic lead-free perovskite solar cells, Mater. Adv. 2 (2021) 754–759, https://doi.org/10.1039/d0ma00860e.

[36] E. Jokar, C.H. Chien, C.M. Tsai, A. Fathi, E.W.G. Diau, Robust tin-based perovskite solar cells with hybrid organic cations to attain efficiency approaching 10%, Adv. Mater. 31 (2019) 1804835, https://doi.org/10.1002/adma.201804835.

[37] X. Liu, T. Wu, C. Zhang, Y. Zhang, H. Segawa, L. Han, Interface energy-level management toward efficient tin perovskite solar cells with hole-transport-layer-free structure, Adv. Funct. Mater. 31 (2021) 2106560, https://doi.org/10.1002/adfm.202106560.

[38] E.W.G. Diau, E. Jokar, M. Rameez, Strategies to improve performance and stability for tin-based perovskite solar cells, ACS Energy Lett. 4 (2019) 1930–1937, https://doi.org/10.1021/acsenergylett.9b01179.

[39] F. Behrouznejad, X. Li, A.A. Umar, X. Zhang, R. Khosroshahi, S.K. Md Saad, I. Ahmed, N. Taghavinia, Y. Zhan, The fingerprint of charge transport mechanisms on the incident photon-to-current conversion efficiency spectra of perovskite solar cells, Sol. Energy Mater. Sol. Cells 253 (2023), 112234, https://doi.org/10.1016/j.solmat.2023.112234.

[40] D. Song, H.Y. Tseng, S. Narra, I.H. Tsai, E. Wei-Guang Diau, Solvent engineering for triple cationic ITO-based mesoscopic tin perovskite solar cells, Chem. Eng. J. 464 (2023), 142635, https://doi.org/10.1016/j.cej.2023.142635.

[41] Z. Guo, A.K. Jena, G.M. Kim, T. Miyasaka, The high open-circuit voltage of perovskite solar cells: a review, Energ. Environ. Sci. 15 (2022) 3171–3222, https://doi.org/10.1039/d2ee00663d.

[42] B. Hailegnaw, N.S. Sariciftci, M.C. Scharber, Impedance spectroscopy of perovskite solar cells: studying the dynamics of charge carriers before and after continuous operation, Phys. Status Solidi Appl. Mater. Sci. 217 (2020) 2000291, https://doi.org/10.1002/pssa.202000291.

[43] E. Von Hauff, D. Klotz, Impedance spectroscopy for perovskite solar cells: characterisation, analysis, and diagnosis, J. Mater. Chem. C 10 (2022) 742–761, https://doi.org/10.1039/d1tc04727b.

[44] S.M. Abdulrahim, Z. Ahmad, J. Bahadra, N.J. Al-Thani, Electrochemical impedance spectroscopy analysis of hole transporting material free mesoporous and planar perovskite solar cells, Nanomaterials 10 (2020) 1635, https://doi.org/10.3390/nano10091635.

[45] A.P. Cismesia, G.R. Nicholls, N.C. Polfer, Amine vs. carboxylic acid protonation in ortho-, meta-, and para-aminobenzoic acid: An IRMPD spectroscopy study, J. Mol. Spectrosc. 332 (2017) 79–85, https://doi.org/10.1016/j.jms.2016.10.020.

[46] S. Shahbazi, C.M. Tsai, S. Narra, C.Y. Wang, H.S. Shiu, S. Afshar, N. Taghavinia, E. W.G. Diau, Ag doping of organometal lead halide perovskites: morphology modification and p-type character, J. Phys. Chem. C 121 (2017) 3673–3679, https://doi.org/10.1021/acs.jpcc.6b09722.